Star Defects, Boojums, and Cardioid Droplet Shapes in Condensed Dimyristoylphosphatidylethanolamine Monolayers

Jordi Ignés-Mullol,* Josep Claret, and Francesc Sagués

Departament de Química Física, Universitat de Barcelona, Martí i Franquès 1, E-08028 Barcelona, Spain

Received: June 2, 2003; In Final Form: August 29, 2003

The inner texture and shape of condensed droplets in Langmuir monolayers of the phospholipid dimyristoylphosphatidylethanolamine (DMPE) have been studied by Brewster angle microscopy. We report a strong temperature dependence of the inner texture in the range 15 °C ≤ T ≤ 25 °C, with continuous distortions and boojums at low temperatures and segmented textures that include 6-fold star defects at high temperatures. Image analysis of metastable $m = 1$ textures at low temperatures has yielded important material parameters. At all temperatures, a clockwise bend structure of the *c*-director is observed. Droplet shapes are typically cardioidlike, becoming more circular for small droplets or high temperatures. This system exemplifies the need for better theoretical models to understand the problem of the formation of complex shapes and textures in condensed Langmuir monolayers.

1. Introduction

Phospholipid monolayers, a model system for the biological membrane, have been studied for many years by exploring the surface pressure/area isotherms. The onset of first-order phase transitions in these monolayers has been confirmed by fluorescence microscopy.[1] The existence of hexatic phases in monolayers of the most usual phospholipid has been proved by X-ray diffraction and is well documented in the literature.[2] Optical techniques such as Brewster angle microscopy (BAM)[3,4] are sensitive to order at mesoscopic length scales and provide indirect evidence of the presence of hexatic order in monolayers. The long-range orientational order results in patterns and textures that, under suitable experimental conditions, include star defects, a clear signature of hexatic order. Such structures have been observed and analyzed in monolayers of phospholipids,[1] fatty acids,[5] alcohols and esters,[6] monoglycerides,[7,8] etc. Techniques such as BAM have occasionally been applied to phospholipid monolayers,[9−12] and experiments suggest a richness in the inner textures of condensed phases of phospholipids similar to what is found in the single-tailed molecules.

A significant effort has been devoted in the last 10 years to understanding the mechanisms that lead to the equilibrium condensed droplet shapes and textures in Langmuir monolayers: a balance between the cost in elastic energy required to include gradients in molecular orientation inside the droplet and the cost in energy to depart from favorable anchoring angles at the boundary with the isotropic phase. This translates into complex textures, which include continuous orientational changes and segmented configurations,[13] and also into boundary shapes that depart from circular, by developing either small protrusions or indentations.[8,14−16] There have been significant attempts at understanding these phenomena, both analytically[17,18] and numerically.[19−21] The analysis of droplet shapes in terms of a competition between line tension and electrostatic repulsion (as introduced by McConnell and co-workers[22,23]) has been recently extended by Krüger and Lösche[24] to include a term in the free energy that favors spontaneous curvature in monolayers of chiral molecules, reproducing patterns and shapes found in some chiral phospholipid monolayers.

In the work reported here, the inner texture and equilibrium droplet shapes in condensed monolayers of the chiral phospholipid DMPE are studied. A qualitative study of this system was reported by Weidemann and Vollhardt.[9] Here, we have employed quantitative BAM image analysis to extract information concerning both the molecular configuration for the observed textures and important material parameters. The observed textures are strongly temperature-dependent: continuous changes in reflectivity are observed at low temperatures, and segmented structures are observed at high temperatures. In all cases, molecular tilt is organized in a clockwise bend configuration (consistent with the chiral nature of the phospholipid). Our observations reveal some contradictions in the existing work that relates the inner texture and the boundary shape of the droplets, indicating the need for more sophisticated physical models.

2. Materials and Methods

L-α-DMPE (1,2-Dimyristoyl-*sn*-glycero-3-phosphatidylethanolamine) was purchased from Sigma (approximately 99% pure) and was used as received. Spread monolayers were prepared by depositing drops of a chloroform (J. T. Baker, p.a. grade) solution (1.5 mg/mL) on the surface of pure water (USF PureLab, 18 MΩ·cm) contained in a custom-built Teflon trough (240 × 80 × 3 mm^3). Temperature in the subphase was controlled to within ±0.2 K by thermoelectric Peltier elements, which exchanged heat with a thermostated water reservoir. A Teflon-encapsulated miniature bead thermistor was used to monitor and control the subphase temperature. The setup is protected inside a 1 m^3 enclosure where air temperature is kept a few degrees above the subphase temperature to prevent the onset of convection currents. The surface area of the trough was adjusted by means of two spring-loaded, motorized Teflon barriers that provided a leak-free enclosure for the monolayer. The surface pressure of the monolayers was monitored with a filter paper Wilhelmy plate attached to a R&K electrobalance. The system was computer-controlled with a National Instruments DAQ board and customized software designed with LabView.

10.1021/jp0355408 CCC: $27.50
Published on Web 11/22/2003

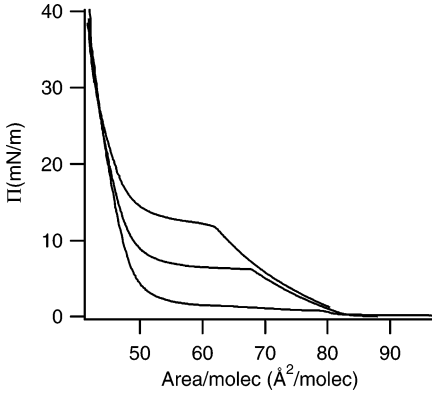

Figure 1. Isotherms of DMPE at the three working temperatures in the present experiments. From bottom to top, curves correspond to $T = 15.0$, 20.0, and 25.0 °C.

Monolayers are initially spread at areas per molecule of about 90 Å^2, which corresponds to either the gas/expanded (G/LE) coexistence region or the LE region, at the desired working temperature. Ten minutes is allowed for complete solvent evaporation and relaxation of the monolayer. Subsequent compression is applied by closing the barriers at a constant rate in the order of 10^{-2} nm^2 molecule^{-1} min^{-1}. Nucleation and growth of the condensed phase (LC) eventually occurs at the onset of the main phase transition (Figure 1). At these compression rates, LC domains grow rather compact, although their perimeter is quite lobulated.[9] If monolayers are allowed to relax at a constant surface area, an equilibrium configuration is attained after typically about 1−2 h, when both the shape and inner texture of condensed nuclei are fully relaxed. Trapped metastable configurations may be obtained by steady compression (without relaxation) past the coexistence region.

Imaging of the monolayer was performed by a custom-built Brewster angle microscope. A mirror placed perpendicularly to the water surface deflects the incident beam prior to reflection on the interface, allowing all optical elements to be placed on the same mechanical arm, which facilitates the setup and adjustment of the instrument. *xyz* Translation is provided for focusing and scanning of the monolayer. Light from a 30-mW 650-nm diode laser is spatially filtered and collimated to the desired beam size prior to being *p*-polarized by a Glan−Thomson prism and is directed toward the air−water interface at an angle close to the Brewster angle ($\theta_B \simeq 53.1°$). The reflected light is focused on a CCD camera (Sony XC-77CE), after passing through a second Glan−Thomson prism, by an $f = 40$ mm lens. The video signal from the camera is stored in a Super-VHS VCR (JVC-S388E) and digitized in 8-bit by a Scion LG-3 frame grabber. Image analysis is performed with the public domain software Image-J. All images include a 100 μm ruler as a reference.

2.1. BAM Image Analysis. Quantitative BAM image analysis has been successfully carried out on monolayers of simpler, single-chain molecules, such as fatty acids,[25,26] on the basis of the assumption that the monolayer behaves as an optically uniaxial medium, locally characterized by an optical axis (the molecular backbone) and two dielectric coefficients ($\epsilon_{||}$ and $\epsilon_{\perp}$). X-ray studies[2] show that DMPE monolayers can be analyzed in terms of the ordering of individual tails, despite their pairwise coupling with one head. We will assume, therefore, that the uniaxial approximation is valid for DMPE monolayers as well. It is known that condensed-phase monolayers are generally characterized by a uniform average molecular polar tilt with respect to the normal to the interface[27] while the azimuth may vary between neighboring regions, causing their reflectivities to be different.[28] This allows us to distinguish different domains in the BAM images.

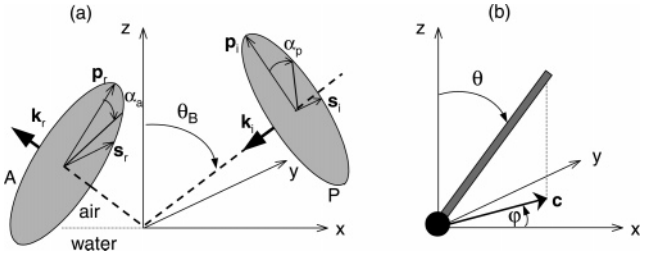

Figure 2. Angular conventions for the polarization of light (a) and for the orientation of the alkyl chains (b). The *p* and *s* components of the polarized light are indicated for the polarizer (P) and the analyzer (A), along with the respective polarization angles (α_p and α_a). The plane of incidence is the *xz* plane. The plane of the BAM images is *xy*, the *x*-axis points north, and the *y*-axis points west.

Uneven illumination of the interface or the unavoidable presence of optical artifacts, such as diffraction rings, would make it difficult to obtain an absolute calibration for the reflected light intensity. Given the chosen camera settings (fixed gain, $\gamma = 1.0$), we have considered a linear relation between the gray-scale distribution in the (background-corrected) BAM images and the calculated reflectivity. Only the shape of the reflectivity curve (reflectivity vs azimuth) will be relevant in our analysis of BAM images because it informs us of the contrast between regions with different molecular orientations. The absolute value of the reflectivities are absorbed by two fitted parameters (gain and offset of the digitization process).

The plane of incidence is perpendicular to the plane of the images shown in this paper, with light moving north to south with respect to these images (Figure 2). The analyzer is rotated to optimize the contrast in the images at an angle close to 60° (counterclockwise as seen by the viewer of the BAM images) with respect to the polarizer, which is aligned with the plane of incidence (Figure 2). With this configuration, the darkest (respectively brightest) regions in the images correspond to molecules tilted toward the left (respectively right) of the viewer (see below). BAM images are shown with their real aspect ratio: a scaling of about 167% [1/cos (θ_B)] has been digitally applied in the vertical direction to correct for the distortion due to the oblique orientation of the camera. For the same reason only a region of about a fourth of the total image is well focused. Nevertheless, for time-independent observations, larger portions of the monolayer have been imaged by digitally assembling a sequence of images that scan the monolayer in the direction of the beam. Gradients in the illumination field and other optical artifacts have been digitally corrected by use of a suitable background function fitted to each image.

Reflectivity from a Langmuir monolayer depends on local molecular orientation, molecular length, and on the coefficients of the dielectric tensor (dielectric susceptibility). In the approximation of a uniaxial anisotropic medium there are only two independent dielectric susceptibilities, and the reflectivity can be evaluated analytically in a straightforward yet tedious calculation.[29,30] A conveniently simple expression may be obtained by taking advantage of the fact that the monolayer is thin compared to the wavelength of light.[25,31] The optical path introduced by the monolayer is proportional to $\delta = 2\pi L \cos(\theta)/\lambda_0$, where L is the length of the hydrophobic tails, θ is the molecular tilt and λ_0 is the wavelength of light in a vacuum. Typically, δ is on the order of 10^{-2}. For incidence with *p*-polarized light, the reflected intensity is expressed as

$$r = |r_{pp} \cos(\alpha_a) + r_{sp} \sin(\alpha_a)|^2 \quad (1)$$

where α_a is the analyzer angle (see Figure 2). The analytical expressions for r_{pp} and r_{sp} may be greatly simplified by obtaining an approximation to order δ^2 for incidence at Brewster angle, namely

$$r_{pp} = \frac{\delta}{2\cos(\theta_B)}\left(1 - \cos(\theta_B)^2 \times \left[\epsilon_\perp + \frac{n^2 + \epsilon_\perp \epsilon_a \cos(\varphi)^2 \sin(\theta)^2}{\epsilon_\perp + \epsilon_a \cos(\theta)}\right]\right) \quad (2)$$

$$r_{sp} = \frac{-\delta\, \epsilon_a \sin(\varphi)\sin(\theta)}{(1+n^2)[\epsilon_\perp + \epsilon_a \cos(\theta)^2]} \times [\epsilon_\perp \cos(\varphi)\sin(\theta) - n\cos(\theta)] \quad (3)$$

Here, $\epsilon_a = \epsilon_{||} - \epsilon_\perp$ is the dielectric anisotropy and n is the index of refraction of water [$\tan(\theta_B) = n$]. The angular parameters are defined in Figure 2. The gray level in the images, R, is related to the reflectivity, r, as

$$R(\theta, \varphi) = R_0 + \Delta R r(\theta, \varphi, ...) \quad (4)$$

where R_0 and ΔR are the offset and gain introduced by the digitization process. These two parameters will be obtained during the fitting of our experimental data, but no information will be extracted from them. It becomes clear from eqs 2 and 3 that the thickness of the layer only contributes a factor, independent of azimuth, to the reflectivity, and it will be absorbed by the fit parameters R_0 and ΔR. Small departures from the ideal conditions (*p*-polarization, Brewster angle) result in corrections to eq 1. Nevertheless, one may verify that they will be absorbed by R_0 and ΔR during the analysis.

3. Results and Discussion

3.1. Continuous Textures at Low Temperatures. Compression at $T = 15$ °C (typically, at a rate of 0.01 nm^2 molecule^{-1} min^{-1}) results in the growth of lobulated LC nuclei with an inner texture characterized by a continuous centrosymmetric change in the reflectivity around a point singularity (Figure 3). The distribution of gray levels about the singularity has a 2π periodicity, which means that the *c*-director performs one full (clockwise, see below) rotation about the singularity (winding number $m = 1$). The structure is analogous to the point defects observed in smectic liquid crystal films.[32] Close inspection of the LC nuclei reveals that the point singularity is always connected to the surrounding LE phase, sometimes only by a narrow fjord (Figure 3). This becomes clear if the BAM analyzer is turned to 0°, the configuration where the LC and LE phases are most contrasted in BAM images (Figure 3b). If compression is stopped and the monolayer is allowed to relax at constant area in the LC/LE coexistence region, the outer perimeter of the droplets becomes smoother. This leads to the progressive opening of the fjord of LE phase (Figure 4). After about 2 h, most LC nuclei have adopted a cardioidlike shape. Relaxation for even longer periods does not result in further significant changes of the droplet shape. A continuous clockwise configuration in the inner texture is preserved at all times.

The $m = 1$ point defect structures (Figures 3 and 4a) can be rendered stable if compression of the monolayer is not stopped until well past the plateau of LC/LE coexistence. Although some metastable LE phase remains for extended periods of time, no significant alteration of the *c*-director structure is observed after compression is halted above the plateau (Figure 5). Moreover, the fjord of LE phase becomes invisibly thin at high compressions. Clearly, the relaxation observed in the coexistence region (Figure 4) requires a significant alteration of the shape of the droplet, which is prevented in the highly condensed states. The stabilized $m = 1$ textures are of significant interest for the purpose of quantitative BAM image analysis. Indeed, they contain a map of the gray level for all possible values of the molecular azimuth. This is in contrast with the usual situation when material parameters of lipid monolayers are extracted from quantitative BAM image analysis of structures with star defects,[26] where only a limited number of gray levels can be obtained simultaneously, and experimental uncertainty in the measured reflectivity and corresponding estimated azimuth angles may have a significant impact on the fitted parameters.

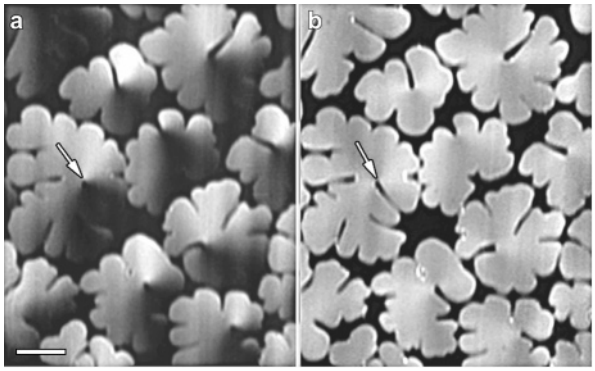

Figure 3. At $T = 15$ °C, LC droplets condense with an inner structure characterized by continuous reflectivity changes around a point defect inside the droplet. All nuclei are condensed with a fjord of LE phase that reaches the defect. Under the usual conditions of analyzer at 60° (a), fjords in the bottom-right quadrant are not visible, but they are exposed if the analyzer is turned to 0°, as in the example pointed to by the arrow (b). The line segment is 100 μm long.

The assumption of radial symmetry has been verified by comparing the distribution of gray levels inside concentric annular regions of increasing radius. Image analysis is carried out by fitting the angular distribution of gray levels to eq 4. On top of the two parameters coming from the linear transformation, R_0 and ΔR, four other parameters are fitted for a given surface pressure, namely, $\epsilon_{||}$, $\epsilon_\perp$, θ, and ϕ_0, where the *c*-director of the azimuth field is taken to be oriented as $c(\varphi) = [\cos(\varphi), \sin(\varphi)]$ with $\varphi = \phi - \phi_0$, ϕ being the angular polar coordinate and ϕ_0 the angle between the molecular azimuth and the radial direction (see Figure 6). The dependence of θ and ϕ_0 on Π has been tested by analyzing the reflectivity of the same region of the monolayer for increasing compression (Figure 6a). For each Π (for a total of nine values) the distributions of gray levels for five nuclei are averaged and fitted as just described. On a first pass, the six parameters listed above are freely adjusted for each data set. The resulting nine pairs of values for the dielectric susceptibilities are averaged, obtaining $\epsilon_{||} = 2.26 \pm 0.02$ and $\epsilon_\perp = 2.18 \pm 0.02$. The value for $\epsilon_\perp$ is consistent with the one reported by Paudler et al.[33] for docosanoic acid monolayers, while our estimate for $\epsilon_{||}$ is significantly lower than the one for docosanoic acid ($\epsilon_{||} \simeq 2.40$). This difference may be attributed to disorder frozen in the condensed phases of the phospholipid.[2] A second pass in the data fit is performed to refine the determination of θ and ϕ_0 with the dielectric susceptibilities constrained to the estimated average values. The orientation of the *c*-director is independent of Π, with $\phi_0 = 108° \pm 5°$, which corresponds to a clockwise bend configuration as illustrated in Figure 6b. The polar tilt is $\theta = 17° \pm 2°$ for Π

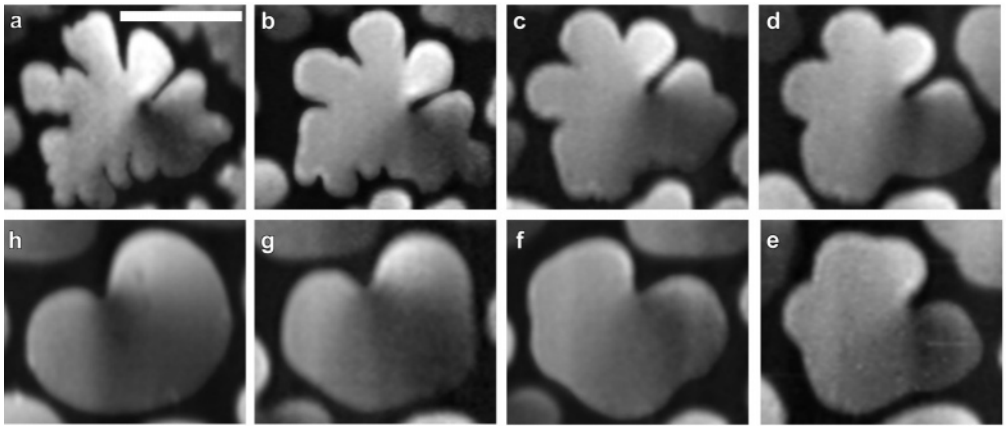

Figure 4. Constant area relaxation of a condensed droplet at $T = 15$ °C after compression is stopped at $\Pi = 4.0$ mN m^{-1} (a). Elapsed times are $t = 10$ min (b), $t = 20$ min (c), $t = 30$ min (d), $t = 55$ min (e), $t = 70$ min (f), $t = 80$ min (g), and $t = 120$ min (h). The orientation of the droplet varies with time due to small convection currents in the subphase and air currents above. The line segment is 100 μm long.

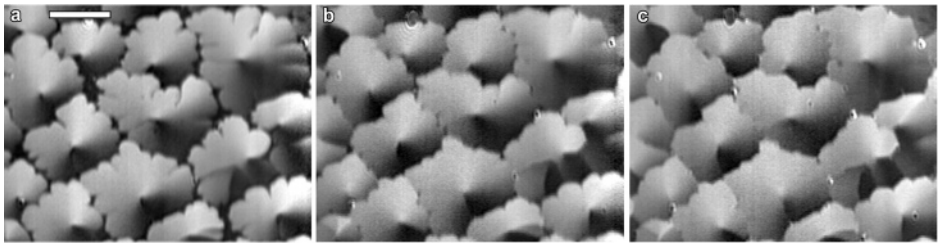

Figure 5. Three stages in the stepwise compression of a DMPE monolayer at $T = 15$ °C. A compression rate of 0.01 nm^2 molecule^{-1} min^{-1} is applied until $\Pi = 6$ mN m^{-1}. Subsequent compression is applied stepwise, at a rate of 5×10^{-3} nm^2 molecule^{-1} min^{-1} alternated with periods of 300 s of relaxation at constant area prior to image acquisition at each Π. Surface pressure is 6.9 mN m^{-1} (a), 13.8 mN m^{-1} (b), or 21.9 mN m^{-1} (c). A significant amount of metastable LE phase is observable in panel a but has disappeared completely in panel b. The line segment is 100 μm long.

< 14 mN/m and decreases steadily for higher Π (Figure 7). These values are consistent with X-ray diffraction results found in ref 2. For the range of Π reported in Figure 7, one would expect a steady decrease of θ upon compression, since the LE/LC coexistence plateau is well under $\Pi = 6$ mN/m (Figure 1). The fact that this does not happen for $\Pi < 14$ mN/m may be justified by the presence of trapped metastable LE phase beyond the plateau region. Compression of the monolayer results in a reduction in the area fraction of metastable LE phase rather than in a reduction of the tilt angle in the LC nuclei. For $\Pi \approx 14$ mN/m, BAM images confirm that condensation of the monolayer is complete (Figure 5) and compression translates into a steady reduction of the molecular tilt. Notice that the radially symmetric texture of the condensed droplets in Figure 5 appears to be independent of the shape of a given nucleus (they all have complex noncircular shapes), showing that bulk elasticity has a dominant contribution in the selection of the inner texture. In this respect, it is remarkable that the *c*-director is approximately normal to the boundary with the LE fjord when in the LC/LE coexistence region (Figure 3). In fact, the presence of the fjord does not alter the $m = 1$ texture.

We will now go back to the analysis of the equilibrium droplet configuration (Figure 4h) using the relevant material parameters determined above.

Unlike in the metastable condensed configuration (Figure 5), the reflectivity pattern is not the same for all droplets in a relaxed monolayer (Figure 8), although equally oriented droplets have equal inner textures. One might assume that no significant changes occur in the *c*-director during the shape relaxation shown in Figure 4. This means that the textures for the relaxed droplets would have a winding number $m = 1$ (just as the freshly condensed droplets have), with the defect near the tip of the indentation. It turns out that constant angle boundary conditions are exactly satisfied on a cardioid if the field has a $m = {}^3/_2$ winding number. In this case the defect should be placed either on the boundary or outside the droplet. On the other hand, a winding number $m = 2$ is typically considered in the analysis of boojum textures since it satisfies constant-angle boundary conditions on a circular droplet with the singularity on the outer perimeter. Departure from circular droplet shapes (just as in the present case) is observed in many monolayer systems, by development of either protrusions or indentations. This is accompanied by the *expulsion* of the singularity from the droplet, thus decreasing the director field gradients and lowering the bulk elastic energy. We have fitted the inner texture of a number of droplets in Figure 8A with those three winding numbers. Regardless of the choice of winding number, our analysis shows that the equilibrium *c*-director closely satisfies constant-angle boundary conditions (nearly tangent, bending clockwise) in the region away from the cusp, but they are clearly violated on the opposite side. Overall, the textures resulting from a fit with $m = 2$ are marginally better at reproducing the experimental ones. The most significant effect of the choice of winding number is the magnitude of the expulsion distance (Figure 8C) required to fit a given texture. While $m = 1$ results in the prediction of a defect placed close to the inward cusp, regardless of the droplet size, $m = 2$ predicts a significant expulsion distance, which increases, relative to the droplet size, for smaller droplets. Experimentally, this translates into smaller reflectivity gradients inside small droplets (Figure 8A). Moreover, we see that larger droplets have a more developed indentation (they are less circular).

The above observations are in agreement with what Rivière and Méunier report for fatty acid monolayers[15] and with the

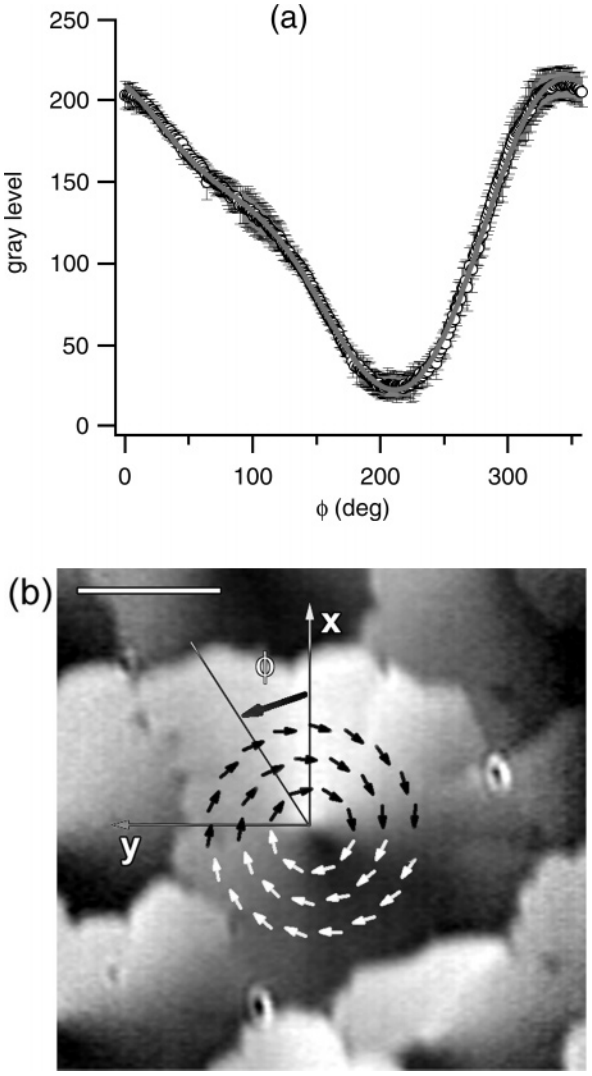

Figure 6. (a) Gray level as a function of the polar angle ϕ (open symbols) averaged over five LC droplets on a DMPE monolayer, $T = 15$ °C, $\Pi = 9.8$ mN m^{-1}, from the series in Figure 4. Error bars equal, at each polar angle, the rms dispersion. The solid line is a fit of the data to the reflectivity curve as described in the text. (b) *c*-Director for a droplet at $\Pi = 15.9$ mN m^{-1}. The line segment is 100 μm long.

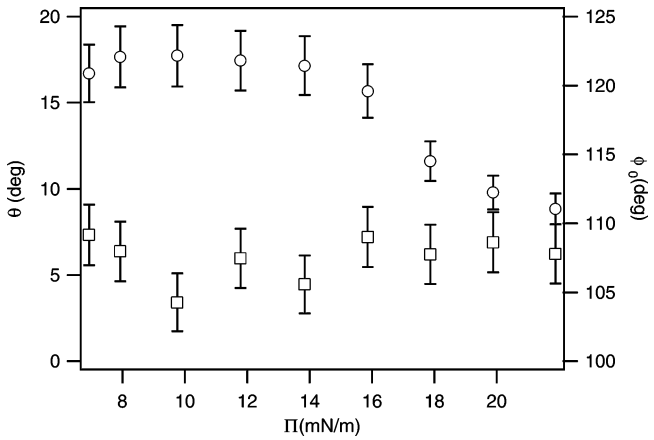

Figure 7. Polar tilt θ (○) and orientation of the azimuth field ϕ_0 (□) as a function of surface pressure, as extracted from the analysis of BAM images, for a DMPE monolayer at $T = 15$ °C.

predictions from the model of Galatola and Fournier.[19] Concerning the relationship between the dented droplet shapes and the clockwise bend inner texture observed in our system, there are contrasting models in the literature. While some authors predict these shapes for bend inner textures,[19] others suggest that they correspond to splay textures.[21] The theoretical framework in these references is all theories for nonchiral molecules. Recently, Krüger and Lösche[24] have considered the role of molecular chirality in condensed droplet shapes. Their approach ignores the effect of the inner texture and determines the shape as an interplay between line tension and bulk electrostatic repulsion.[22,23] They incorporate an extra energy term that accounts for a spontaneous curvature introduced by the arrangement of chiral molecules. Their calculations, which agree with some of their own experiments on chiral lipid monolayers, predict the nucleation of cardioid-shaped, rather than circular, condensed droplets. Experiments by Weidemann et al. with monoglyceride monolayers[9] and by Albalat et al. with diacylglycerol amino acid-based surfactant monolayers,[34] both nonchiral compounds, report the observation of droplets with dented shapes for splay inner textures. Clearly, neither the anisotropy in the bulk elasticity nor the chiral nature of the compound is enough to determine the shape of the droplets, and more sophisticated physical models seem to be needed.

3.2. Appearance of Discontinuous Textures. While mostly continuous textures result from condensation of DMPE monolayers for $T \leq 16$ °C, droplets are divided into segments with different reflectivity for $T > 17$ °C (Figure 9). At $T \simeq 17$ °C, textures share features from both types of configurations: while discontinuities are present in most nuclei, boojum textures are clearly observable, even in nuclei with discontinuities. Transition between neighboring segments is not as sharp for DMPE monolayers as in other well-known systems, such as fatty acids, alcohols, esters, or monoglycerides.[6,7,9] Moreover, we observe that the number and organization of these segments is very irregular in DMPE monolayers, consistent with the textures reported by Weidemann and Vollhardt.[9] Segments have a uniform gray level for $T \geq 25$ °C but they exhibit reflectivity gradients for lower temperatures (Figure 9). Lines that separate two neighboring segments are often kinked, with angles in the vicinity of 120° (see Figure 9c). Lines are organized so that three or more meet at one point, often at the droplet boundary. When this happens, it coincides with an indentation in the boundary shape, in analogy with the organization of monoglyceride monolayers,[9] resulting in a shape not unlike what we have described for the lower temperature configurations.

The difference in the inner texture of condensed droplets below $T = 16$ °C and above $T = 17$ °C is not the result of domain relaxation. Indeed, nuclei growing above $T = 17$ °C exhibit sharp discontinuities in their inner texture already upon nucleation. Although their lobulated contour shape is analogous to that observed at $T = 15$ °C, the difference in the inner structure is immediately noticeable. Figure 10 shows the constant area isothermal relaxation of a LC droplet in the LC/LE coexistence region at $T = 25$ °C. Notice that changes with time involve mostly the smoothing of the LC/LE interface, while the inner structure remains roughly unaltered, preserving the identity of the constant reflectivity segments. The physical reality of the defect lines is reaffirmed thanks to the variations in the orientation of the droplets. When a nucleus rotates (compare frames b−d in Figure 10) the gray level of a given segment, as perceived by the BAM, changes accordingly (in fact, this shows that viscous drag with the subphase or the surrounding LE phase does not alter the *c*-director), i.e., line discontinuities appear invariant under different orientations with respect to the plane of incidence.

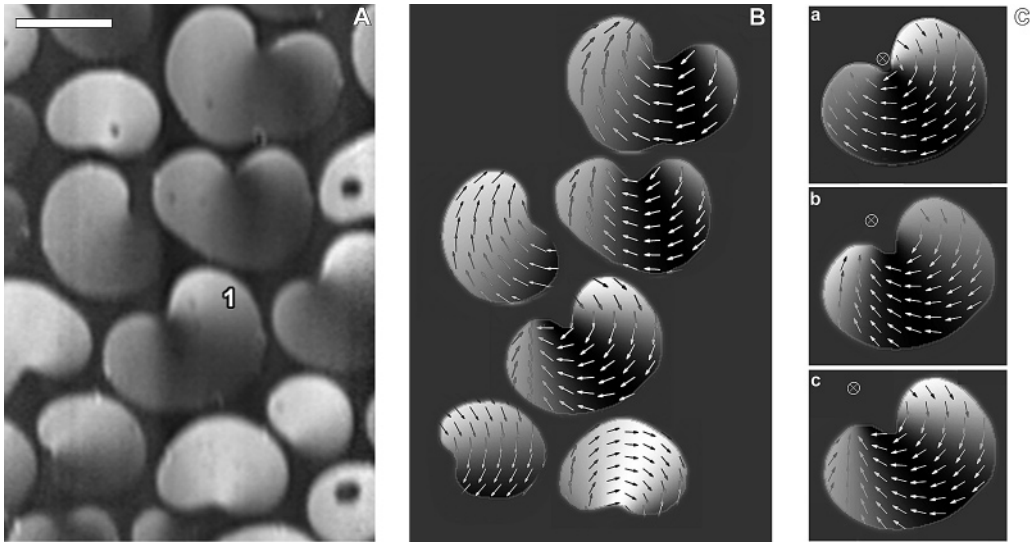

Figure 8. DMPE monolayer kept at constant area at $T = 15$ °C, $\Pi = 4.3$ mN/m for 120 min (A). The inner structure of the cardioid-shaped condensed nuclei is consistent with a continuous bend distortion of the *c*-director. The textures can be best fitted with a $m = 2$ bend texture centered outside of the nucleus (B). The only fit parameters are the position of the defect and the orientation of the director field with respect to the horizontal. The position of the singularity determined for the droplet labeled 1 is illustrated in panel C for the three winding numbers, namely, $m = 1$ (a), $m = {}^3/_2$ (b), and $m = 2$ (c). The line segment in panel A is 100 μm long.

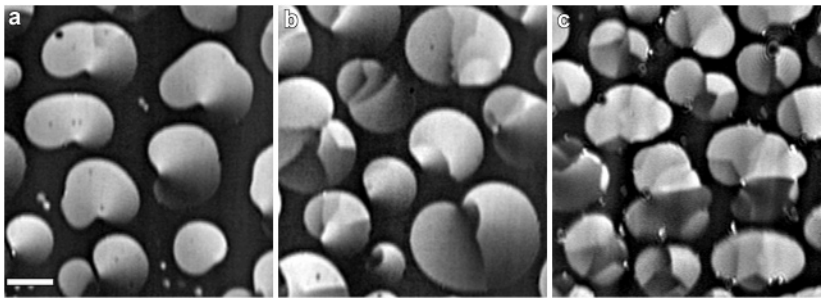

Figure 9. DMPE monolayers after constant area relaxation for 60 min at different temperatures: $T = 16.0$ °C, $\Pi = 3.5$ mN/m (a); $T = 17.0$ °C, $\Pi = 4.6$ mN/m (b); and $T = 20.0$ °C, $\Pi = 8.0$ mN/m (c). While textures in panel a are characterized by continuous modulations of the *c*-director, those in panel c contain walls across which there is an abrupt change in reflectivity. Textures in panel b appear to be a transition between the two regimes. Boundary shapes with an inverted cusp are observable at all temperatures. The line segment is 100 μm long.

Star defects with a regular 6-fold structure may form when the meeting point of six segments is close to the center of a droplet (Figure 11). This occurs noticeably at $T = 25$ °C and above, while they are scarce below this temperature (Weidemann and Vollhardt[9] did not report any observation of these very regular structures in their experiments at $T = 23$ °C). Only when exactly six segments meet inside a droplet does such a regular configuration form. Analysis of the distribution of gray levels as a function of the polar angle around the central star defect shows a profile that is compatible with that observed at low temperatures (Figure 6). The director field is roughly constant inside each segment and oriented perpendicular to the bisector, thus describing a clockwise bend about the central singularity (Figure 11).

The fact that significantly different inner structures result in the condensation of DMPE monolayers as a function of temperature suggests the possibility of observing a structural transition between the two configurations. We have performed controlled temperature quenches of ± 10 °C starting from the equilibrium configuration at both 15 and 25 °C. The rate of temperature variation has been kept at ± 0.1 °C/min, to minimize the build-up of temperature gradients. Surface pressure has been adjusted for each temperature to maintain approximately constant the compressibility modulus, as determined from the isotherms, to keep the size of the LC nuclei roughly constant during the quench. We have been unable to detect significant changes during or after the quenches. Indeed, star defects formed at $T = 25$ °C have remained unperturbed after hours at temperatures as low as $T = 10$ °C, and droplets with continuous textures formed at $T = 15$ °C have not developed segments at high temperatures.

4. Conclusions

We have presented a study of the inner textures and condensed droplet shapes of DMPE monolayers based on the analysis of BAM images. We have observed a clear temperature dependence of the droplet textures: the *c*-director changes continuously for $T \leq 16$ °C, while segmented textures are observed for $T \geq 17$ °C. At even higher temperatures, regular 6-fold star defects are observed. At all temperatures and surface pressures, BAM image analysis shows that the texture is consistent with a clockwise bend configuration of the *c*-director, reflecting the chiral nature of the compound. Upon nucleation, low-temperature droplets develop a continuous centrosymmetric texture with a $m = 1$ singularity near the center. This structure can be stabilized if the monolayer is compressed past the LC/LE coexistence region. From our analysis we have also obtained the polar tilt at each pressure and the dielectric coefficients. Values of the polar tilt are consistent with those determined by X-ray diffraction,[2] namely, $\theta = 17°$ in the coexistence region. Moreover, a steady decrease of θ is detected upon compression

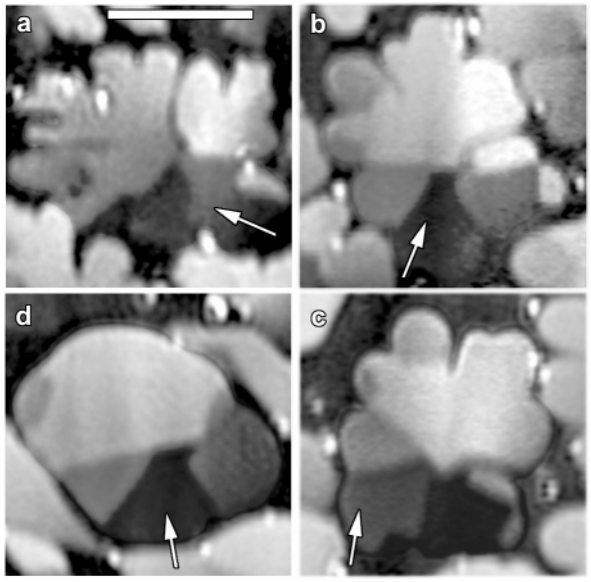

Figure 10. Constant area relaxation of a condensed droplet at $T = 25$ °C after compression is stopped at $\Pi = 15.0$ mN m^{-1} (a). Elapsed times are $t = 10$ min (b), $t = 16$ min (c), and $t = 50$ min (d). The arrow identifies a sector in the inner structure as it changes its apparent reflectivity when the orientation of the nucleus varies. The line segment is 100 μm long.

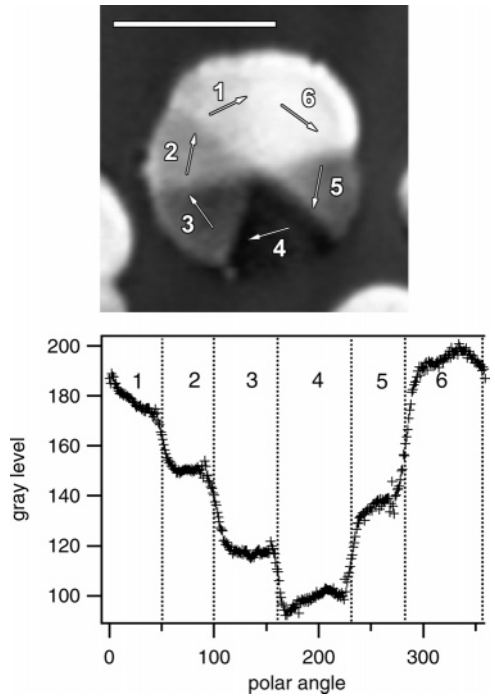

Figure 11. DMPE droplet at $T = 25$ °C, $\Pi = 13.8$ mN/m, after 90 min of relaxation at constant area, with a nucleus exhibiting a 6-segments star defect. The polar distribution of gray levels shows that the reflectivity is roughly constant inside the segments. The structure of the *c*-director, as deducted from the BAM analysis, is shown on the image. The line segment is 100 μm long.

only when no metastable LE phase is observed in the BAM images. The values for the dielectric coefficients are consistent with those reported in the literature for fatty acids,[33] although DMPE monolayers appear to have a lower dielectric anisotropy.

If low-temperature condensed droplets are allowed to relax in the LC/LE coexistence region, their initially lobulated shape becomes smoother, evolving toward a dented circular (cardioid) shape. In the process, the singularity in the *c*-director is expelled outside of the droplet. The shape is markedly more circular for the smaller droplets. If the inner texture is modeled with a $m = 2$ winding number, the defect expulsion distance is determined to increase inversely with the droplet size. The relationship between droplet texture and shape has been analyzed theoretically in recent years. While some authors predict indentations for bend textures[19] (in agreement with the present case) others predict the indentation for splay textures.[21] Besides this theoretical framework, other authors attempt to explain the observed droplet shapes, ignoring the details of the inner texture.[22,23] Recently, the incorporation of a spontaneous curvature term in the free energy for condensed droplets of chiral molecules has resulted in the prediction of dented droplet shapes.[24] Taking into account that we have observed similar shapes for DMPE droplets with continuous and segmented textures, and the reported observations of dented droplets for splay textures of nonchiral molecules,[8] it seems clear that better physical models are needed to fully understand this problem.

The existence of continuous equilibrium textures at low temperatures and segmented ones (even star defects) at higher temperatures in DMPE monolayers remains unexplained. Hexatic order is known to exist in condensed droplets at all studied temperatures.[2] Continuous textures imply that the lock-in energy between the hexatic and azimuth degrees of freedom has a dominant contribution in the elastic energy.[13] The cost in energy to have a continuous distortion of the hexatic field increases with the hexatic stiffness, K_6. Therefore, a large enough stiffness would favor the formation of segmented structures. Given the fact that, typically, K_6 increases inversely with T, the above argument is in contradiction with our observations, since it would predict continuous textures for higher, rather than lower, temperatures. In this discussion, the effect of the headgroup has been ignored. It is expected that a certain degree of orientational order of the headgroups exists, although not quite compatible with the chain lattice. This is assumed to be the reason for the high area per tail measured by X-ray diffraction[2] and for anomalous features in DMPE isotherms.[35] It is plausible that the temperature dependence of the inner textures is closely related to changes in the headgroup ordering, or in its coupling with the hexatic lattice, although no experimental evidence for this exists.

Acknowledgment. We acknowledge financial support from SEID Project BXX2000-0638-C02-01 and DURSI Project 2001SGR00045. J.I.-M. acknowledges financial support from Generalitat de Catalunya, RED-2000 program. We thank D. Vollhardt and Th. Fischer for helpful discussions.

References and Notes

(1) Moy, V. T.; Keller, D. J.; Gaub, H. E.; McConnell, H. M. *J. Phys. Chem.* **1986**, *90*, 3198−3202.
(2) Kenn, R. M.; Kjaer, K.; Möhwald, H. *Colloids Surf. A* **1996**, *117*, 171−181.
(3) Hénon, S.; Méunier, J. *Rev. Sci. Instrum.* **1991**, *62*, 936−939.
(4) Hönig, D.; Möbius, D. *J. Phys. Chem.* **1991**, *95*, 4590−4592.
(5) Hénon, S.; Méunier, J. *J. Chem. Phys.* **1993**, *98*, 9148−9154.
(6) Qiu, X.; Ruiz-García, J.; Stine, K. J.; Knobler, C. M. *Phys. Rev. Lett.* **1991**, *67*, 703−706.
(7) Gehlert, U.; Weidemann, G.; Vollhardt, D. *J. Colloid Interface. Sci.* **1995**, *174*, 392−399.
(8) Brezesinski, G.; Scalas, E.; Struth, B.; Möhwald, H.; Bringezu, F.; Gehlert, U.; Weidemann, G.; Vollhardt, D. *J. Phys. Chem.* **1995**, *99*, 8758−8762.
(9) Weidemann, G.; Vollhardt, D. *Thin Solid Films* **1995**, *264*, 94−103.
(10) Weidemann, G.; Vollhardt, D. *Colloids Surf. A* **1995**, *100*, 187−202.
(11) Weidemann, G.; Vollhardt, D. *Biophys. J.* **1996**, *70*, 2758−2766.

(12) Siegel, S.; Vollhardt, D.; Brezesinski, G.; Bringezu, F.; Mohwald, H. *Mater. Sci. Eng. C* **1999**, *8*−*9*, 3−11.
(13) Fischer, T. M.; Bruinsma, R. F.; Knobler, C. M. *Phys. Rev. E* **1994**, *50*, 413−28.
(14) Schwartz, D. K.; Tsao, M. W.; Knobler, C. M. *J. Chem. Phys.* **1994**, *101*, 8258−8261.
(15) Rivière, S.; Méunier, J. *Phys. Rev. Lett.* **1995**, *74*, 2495−2498.
(16) Fang, J. Y.; Teer, E.; Knobler, C. M.; Loh, K. K.; Rudnick, J. *Phys. Rev. E* **1997**, *56*, 1859−1868.
(17) Rudnick, J.; Bruinsma, R. *Phys. Rev. Lett.* **1995**, *74*, 2491−2494.
(18) Rudnick, J.; Loh, K. K. *Phys. Rev. E* **1999**, *60*, 3045−3062.
(19) Galatola, P.; Fournier, J. B. *Phys. Rev. Lett.* **1995**, *75*, 3297−3300.
(20) Loh, K. K.; Rudnick, J. *Phys. Rev. Lett.* **1998**, *81*, 4935−4938.
(21) Loh, K. K.; Rudnick, J. *Phys. Rev. E* **2000**, *62*, 2416−2427.
(22) Keller, D. J.; McConnell, H. M.; Moy, V. T. *J. Phys. Chem.* **1986**, *90*, 2311−2315.
(23) McConnell, H. M.; Keller, D.; Gaub, H. *J. Phys. Chem.* **1986**, *90*, 1717−1721.
(24) Krüger, P.; Lösche, M. *Phys. Rev. E* **2000**, *62*, 7031−7043.
(25) Overbeck, G. A.; Hönig, D.; Möbius, D. *Thin Solid Films* **1994**, *242*, 213−219.
(26) Tsao, M. W.; Fischer, T. M.; Knobler, C. M. *Langmuir* **1995**, *11*, 3184−3188.
(27) Möhwald, M.; Kenn, R. M.; Degenhardt, D.; Kjaer, K.; Als-Nielsen, J. *Physica A* **1990**, *168*, 127−139.
(28) Kaganer, V. M.; Möhwald, H.; Dutta, P. *Rev. Modern Phys.* **1999**, *71*, 779−819.
(29) Berreman, D. W. *J. Opt. Soc. Am.* **1972**, *62*, 502−510.
(30) Bethune, D. S. *J. Opt. Soc. Am. B* **1991**, *8*, 367−373.
(31) Tabe, Y.; Yokoyama, H. *Langmuir* **1995**, *11*, 699−704.
(32) Pindak, R.; Young, C. Y.; Meyer, R. B.; Clark, N. A. *Phys. Rev. Lett.* **1980**, *45*, 1193−1196.
(33) Paudler, M.; Ruths, J.; Riegler, H. *Langmuir* **1992**, *8*, 184−189.
(34) Albalat, R.; Claret, J.; Ignés-Mullol, J.; Sagués, F.; Morán, C.; Pérez, L.; Clapés, P.; Pinazo, A. *Langmuir*, in press.
(35) Flörsheimer, M.; Möhwald, H. *Colloids Surf.* **1991**, *55*, 173−189.